

Coupled electron-nuclear wavepacket dynamics in potassium dimers

Hendrike Braun¹, Tim Bayer², Cristian Sarpe¹, Robert Siemering³,
Regina de Vivie-Riedle³, Thomas Baumert¹ and Matthias Wollenhaupt⁴

¹ Institut für Physik und CINSaT, Universität Kassel, Heinrich-Plett-Str. 40, D-34132 Kassel, Germany

² Department of Physics of Complex Systems, Weizmann Institute of Science, Rehovot 76100, Israel

³ Department Chemie, Ludwig-Maximilians-Universität München, Butenandt-Str. 11, D-81377 München, Germany

⁴ Institut für Physik, Carl von Ossietzky Universität Oldenburg, Carl-von-Ossietzky-Str. 9-11, D-26129 Oldenburg, Germany

E-mail: matthias.wollenhaupt@uni-oldenburg.de

Received 23 December 2013, revised 17 March 2014

Accepted for publication 20 March 2014

Published 10 June 2014

Abstract

Recently we have demonstrated control of valence-bond excitation of a molecule due to the interplay of the induced charge oscillation with the precisely tailored phase of the driving laser field (Bayer *et al* 2013 *Phys. Rev. Lett.* **110** 123003). In this contribution we describe in more detail the two-colour experiment—a control pulse sequence followed by an ionizing probe pulse of a different wavelength. We provide details on the quantum dynamics simulations carried out to reproduce and to analyse the experimental results. The procedure for averaging over the focal intensity distribution in the interaction region and the method for orientation averaging, which are both crucial for the reproduction of our strong-field measurements, are also described in detail. The analysis of the temporal evolution of the expectation values of the wavepackets on the relevant potentials, the induced energetic shifts in the molecule and the modulation in the charge oscillation provides further insights into the interplay of the coupled nuclear-electron dynamics. Because the measured photoelectron spectra reveal the population of the target states we describe the quantum mechanical approach to calculate the photoelectron spectra and rationalize the results using Mulliken's difference potential method.

Keywords: strong-field control on molecules, ultrafast pulse shaping, coherent electron wavepackets, coupled electron-nuclear dynamics, selective population of dressed states

 Online supplementary data available from stacks.iop.org/JPhysB/47/124015/mmedia

(Some figures may appear in colour only in the online journal)

1. Introduction

The ability to control the course and the outcome of chemical reactions using coherent light as a photonic reagent has been a long-term dream of physicists and chemists alike [1], since the invention of the laser in the 1960s. However, it was not until the development of ultrafast pulsed laser technologies, that active manipulation of photochemical processes could be implemented successfully in the presence of rapid intra-molecular energy redistribution processes. The field of femtochemistry [2] delivered invaluable insights into these ultrafast internal molecular processes and paved the way

to a detailed understanding of molecular reaction dynamics. The interaction of femtosecond laser pulses with matter (at a microscopic level) takes place on the natural time scale of *nuclear* motions, which are at the heart of any chemical reaction. Over the recent years even shorter laser pulses, with pulse durations extending into the sub-femtosecond, i.e. the attosecond time regime, became experimentally available [3–5]. The emerging field of attosecond science opened the door to the measurement of even faster *electronic* processes, since attosecond laser pulses interact with matter on the intrinsic time scale of electron motions in atoms and molecules.

The beauty of those time-resolved experiments lies in our ability to *in situ* observe such ultrafast processes as they occur. However, one is by no means restricted to mere observation but rather seeks to actively exert control on these very processes. With the advent of sophisticated pulse shaping techniques [6, 7] effective directed manipulation of photoinduced dynamics became feasible [8]. At present a shaping precision down to the zeptosecond regime is readily achieved [9].

Due to the high frequency (XUV) and correspondingly high photon energy inherent to attosecond laser fields, these pulses generally address inner shell electrons. Excitations of outer shell electrons by attosecond laser fields suffer from inefficient cross-sections and are likely to cause direct photoionization. Here we focus on the control of valence-bond chemistry, i.e. steering of nuclear motions along different reaction pathways by optical excitation within the neutral system. Electron dynamics involving a coherence with the ground state allow for the fastest conceivable control in valence chemistry, since they make use of the highest available energy level spacings. Electronic transitions driven by optical, i.e., pico- to femtosecond laser pulses benefit from large transition moments, being a prerequisite for efficient population transfer. In addition, the application of non-perturbative interactions associated with intense laser fields is mandatory in order to achieve efficient product yields. Strong laser fields inherently alter the potential energy surfaces (PESs) via AC-Stark shifts and thereby open up new reaction pathways to target states that are inaccessible in the weak-field regime [10–13]. The non-resonant dynamic Stark effect acts on the time scale of the intensity envelope of an ultrashort laser pulse [14]. It offers for example the observation of non-Franck–Condon transitions in bound wavepacket motion [16], population control in atoms by shaped laser pulses [17], control of bound vibrational levels [18], and control of the branching ratio in a dissociation reaction [19]. The *resonant* Stark effect on the other hand acts on the time scale of the electron dynamics. Moreover it provides more efficient manipulation of the potential energy landscape. In particular it enables bidirectional Stark shifting of molecular states of several 100 meV to higher as well as lower energies [15]. Although attosecond laser pulses are an excellent tool for the observation of ultrafast processes, they may not be the first choice for the control of valence-bond chemistry—mainly due to the photon energy mismatch. Here we discuss a coherent control scheme based on intense femtosecond laser pulses which are shaped with attosecond precision. The scheme is universally usable and has been the subject of theoretical studies [20, 21]. In a generic scenario, a moderately strong preparatory pulse resonantly couples the ground state with an excited electronic state of different parity, creating a coherent electronic superposition. The induced electron dynamics may equivalently be considered as an electronic wavepacket, a charge oscillation or an oscillating electric dipole-moment. In either case the oscillation period is determined by the carrier frequency of the driving field, around 2.7 fs for typical ultrafast infrared lasers. In the second step of the interaction an intense main pulse, suitably timed with sub-cycle precision, couples to the electron wavepacket and steers the system efficiently towards a preselected electronic

target channel. The phase relation between induced dipole and driving electric field determines whether the interaction energy is increased or decreased, resulting in selection of either a higher or lower energy target channel, both of which entail different nuclear dynamics. The underlying physical mechanism was termed photon locking (PL) in analogy to spin locking well-known from nuclear magnetic resonance. PL was recently discussed in the framework of selective population of dressed states (SPODS) on atomic systems [22].

Recently, the observation and control of coherent charge oscillations has attracted considerable interest [23, 24].

In preceding publications [25, 26] we reported on the active manipulation of the interplay between an induced charge oscillation and the driving laser field. The bespoke tailoring of IR femtosecond laser pulses by spectral phase modulation enabled us to selectively and efficiently excite a molecule into predefined neutral target channels. In this paper we elaborate on the experimental and theoretical approaches and give a detailed analysis of the quantum dynamics induced in the potassium dimer. In particular we establish the picture of a driven charge oscillation as a suited description of strong-field effects.

2. The basic control scheme

To elucidate the physical mechanism behind SPODS [27] we consider a generic double pulse scenario, where both pulses are tuned to an electronic resonance of the molecule [12, 20, 28]. The first pulse serves to excite the molecule and prepares a state of maximum electronic coherence. Quantum mechanically this coherent superposition of ground and excited state represents an electronic wavepacket consisting of states with different parity. Since the energy spacing of the involved quantum states is in the order of several eV, the timescale associated with the electronic wavepacket dynamics is the attosecond to few femtosecond timescale. Therefore, in contrast to vibrational dynamics, the electron dynamics are sensitive to the oscillating electric field itself rather than the electric field envelope. Classically, the electronic coherence represents an oscillating charge distribution in space and time, i.e. an oscillating dipole $\mu(t)$. In analogy to classical physics, the driven dipole follows the resonant driving field $E(t)$ with a phase shift of $\pi/2$ during the excitation. The total energy of the interacting system is given by

$$\epsilon(t) = -\vec{\mu}(t) \cdot \vec{E}(t). \quad (1)$$

This interaction energy depends on the amplitudes of field and dipole as well as the phase relation between both. If the second pulse is in phase with the first, it inherits the $\pi/2$ phase relation to the induced dipole—provided the oscillating dipole is not subjected to additional phase dynamics which we will address later on. In this constellation the time average of the interaction energy is zero which, in a quantum mechanical framework, is equivalent to the equal population of upper and lower light induced potential (LIP—light-induced potentials are the molecular equivalent to dressed states in level systems). However, if the second pulse is phase-shifted by $-\pi/2$ with respect to the first it couples to the coherence out-of-phase

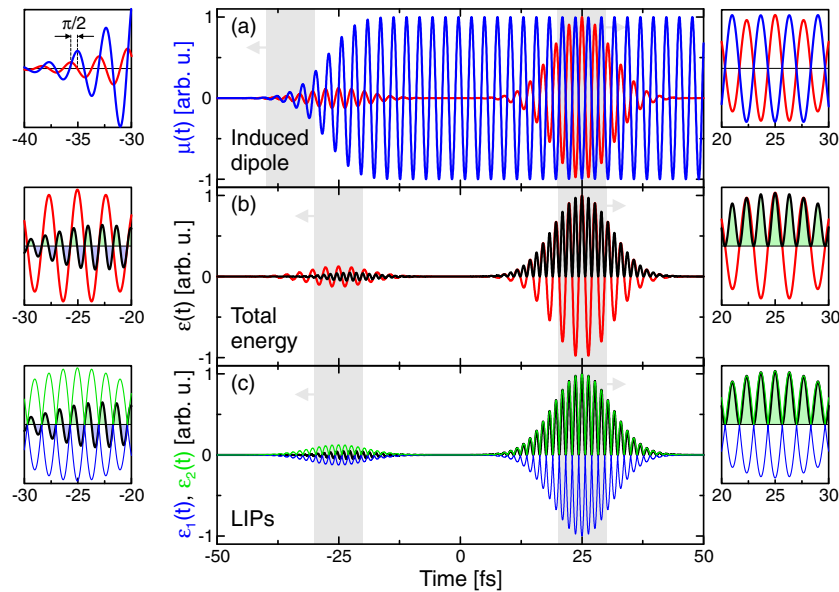


Figure 1. Visualization of the control scenario for a two-level system. (a) The resonant electric field $E(t)$ (red) induces a dipole-moment $\mu(t)$ (blue), whose oscillation follows the driving field with a phase difference of $-\pi/2$, see also inset on the left. If the second pulse is shifted in phase by $\pi/2$ with respect to the first pulse it will couple exactly out-of-phase into the persistent dipole-oscillation, cf right inset. (b) During the first excitation of the dipole-moment the interaction energy $\epsilon(t)$ (black) averages to zero over one oscillation, as can be seen in the inset on the left side. However during the second pulse, when electric field and dipole oscillate with a phase difference of π the interaction energy is maximized and strictly positive, cf right inset. (c) Comparison of the total energy of the interacting system (black) and the energies of the upper and lower LIP (green and blue). During the main pulse the total energy coincides with the energy of the upper LIP, see also right inset.

and thus maximizes $\epsilon(t)$. This maximization of the interaction energy is equivalent to the selective population of the upper LIP [12, 29]. As a result of the increased energy, higher lying molecular target states which are inaccessible in the weak-field limit can now be reached efficiently. Vice versa, if the second pulse couples to the coherence in phase, the interaction energy is minimized implying that the lower LIP is populated selectively. This energy decrease opens up routes to lower lying target states which are non-resonant under weak-field excitation.

For clarity, the described double-pulse scenario is shown in figure 1 for the simplified case of a two-level-system, i.e. no vibrational dynamics are considered. The resonant electric field (red) induces an electric dipole-moment (blue) in the system, that will follow the excitation with a phase difference of $-\pi/2$, as can be seen in frame (a). The second pulse is shifted by $\pi/2$ with respect to the first and couples out-of-phase to the induced dipole-moment. As a consequence the interaction energy, as plotted in frame (b), is maximized during the interaction with the second pulse. This is equivalent to the selective population of the upper LIP in the system. Frame (c) compares the total energy $\epsilon(t)$ to the lower ($\epsilon_1(t)$) and upper ($\epsilon_2(t)$) LIP of the interacting system. While the total energy oscillates around zero during the interaction with the first pulse it coincides with the energy of the upper LIP during the main pulse, verifying the selective population of the upper LIP. The underlying mechanism was termed SPODS as it was first discussed for the dressed states in atoms [27].

In general the situation in molecules will be more complicated due to the nuclear dynamics which are launched along with—and strongly coupled to—the electron dynamics. The amplitude of the electric dipole, and hence the magnitude

of the interaction energy, depends on the overlap of the nuclear wavepackets in the ground and excited state. Efficient and selective control of the electron dynamics requires a maximum overlap of the nuclear wavepackets. Moreover, the nuclear wavepacket propagation generally leads to a continuous variation of the electronic resonance condition. This change in the eigenfrequency of the electric dipole results in a phase drift of $\mu(t)$ with respect to $E(t)$. The laser field has to adapt to this additional phase dynamics if it is to maintain a defined phase relation to the dipole. Therefore, a simple double pulse sequence is not expected to be optimal for efficient control of the coupled electron-nuclear dynamics in molecules. Instead we employ laser fields that are more versatile in terms of amplitude and phase. These fields are generated by phase modulation of the spectrum of an ultrashort laser pulse [6] with a periodic spectral phase of the form

$$\varphi(\omega) = A \sin[(\omega - \omega_0)T + \phi]. \quad (2)$$

In general, sinusoidal spectral phase modulation results in a multipulse sequence in the time domain [30–32]. The relative intensity of the subpulses is controlled by the modulation depth A , whereas their temporal separation is determined by the sine-frequency T . If T is larger than the temporal width ΔT of the input pulse, the subpulses are well-separated in time. If T is smaller than ΔT the subpulses merge, forming a single chirped pulse. The sine-phase ϕ controls the temporal phase of the shaped pulse. It is the most important parameter for the manipulation of the phase relation between induced dipole and laser field. In summary, the pulse parameterization described by (2) provides a great variety of tailored laser fields ranging from regularly shaped multipulse sequences to complex shaped single pulses. Due to this versatility

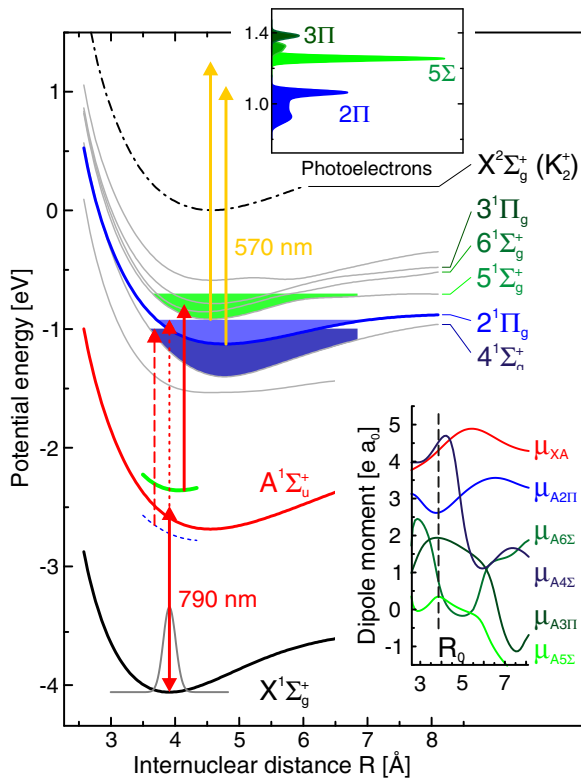


Figure 2. Potential energy surfaces (PES) and electric dipole-moments of the potassium dimer. In the weak-field regime the absorption of two photons leads to an excitation of the $2^1\Pi_g$ state. For intense laser fields the strong coupling of the $X^1\Sigma_g^+$ and the $A^1\Sigma_u^+$ state results in a dynamic Stark splitting in the two-state subsystem as indicated by the line segments around the $A^1\Sigma_u^+$ state around $R = 3.9$ Å. In addition to the $2^1\Pi_g$ state also the $4^1\Sigma_n^+$ state can be reached from the lower LIP. Population in the upper LIP can be transferred into the electronic states $5^1\Sigma_g^+$, $6^1\Sigma_g^+$ and $3^1\Pi_g$ that cannot be reached in the weak-field case. The splitting and the population of the LIPs are closely related to the interaction energy of the driving laser field with the light-induced dipole-moment between the $X^1\Sigma_g^+$ and the $A^1\Sigma_u^+$ state. Manipulating the interaction energy according to (1) allows for control over the population in the electronic target states. A maximization of the interaction energy and the population of the upper LIP in the $X^1\Sigma_g^+-A^1\Sigma_u^+$ system, as suggested by the thick, green line segment above the $A^1\Sigma_u^+$ state, will result in the population of the upper target channel (green-shaded states). The photoelectrons produced in the ionization of the molecule by a second laser pulse with a central wavelength of 570 nm serve as a measure for the population in the target channels. The inset in the lower right part shows the electric dipole couplings between the relevant states.

sinusoidally phase-modulated laser pulses are well-suited to adapt to the richness of dynamics and processes encountered in complex molecular systems.

3. The physical system

As a molecular prototype system we chose the potassium dimer (K_2). We can treat this molecule experimentally and theoretically on an equally accurate level, and it has been the object of previous studies [20, 21, 33]. The PESs and dipole couplings between the relevant states are displayed in figure 2. Shown are only the relevant states accessible by

electric dipole transitions. Before the interaction with the laser the molecule resides in its ground state $X^1\Sigma_g^+$ as suggested by the Gaussian shaped wave function in the sketch. When irradiated with a weak resonant laser field population will flow via the $A^1\Sigma_u^+$ state to the $2^1\Pi_g$ state by a resonant two-photon absorption. Higher lying electronic states such as $5^1\Sigma_g^+$, $6^1\Sigma_g^+$ and $3^1\Pi_g$ are energetically inaccessible. Upon irradiation with a *strong* resonant laser however an electronic coherence between the $X^1\Sigma_g^+$ state and the $A^1\Sigma_u^+$ state is formed, i.e. a charge oscillation is launched by the laser field. Due to the strong coupling between the states the LIPs (indicated by the blue and green line segments above and below the $A^1\Sigma_u^+$ state around the equilibrium internuclear separation R_0) split up in analogy to the dressed states in the atomic case. If the intensity of the driving laser field is strong enough, i.e. the splitting induced in the $X^1\Sigma_g^+-A^1\Sigma_u^+$ system is sufficiently high, population can also be transferred to the higher lying states $5^1\Sigma_g^+$, $6^1\Sigma_g^+$ and $3^1\Pi_g$. In the case of resonant excitation with a bandwidth limited (BWL) pulse both LIPs are populated equally. Therefore no selectivity between the bound electronic target states is achieved. Although the presented description suggests, that dressing of the molecular states and the formation of LIPs does only occur in the subsystem consisting of the $X^1\Sigma_g^+$ and the $A^1\Sigma_u^+$ state, actually the whole system is dressed. As the coupling in the $X^1\Sigma_g^+-A^1\Sigma_u^+$ subsystem is higher than the coupling of the $A^1\Sigma_u^+$ state to the higher lying target states the dressing will affect the target states much less than the $X^1\Sigma_g^+$ and the $A^1\Sigma_u^+$ state. For simplicity we omitted the dressing of the target states in the preceding description. However, the simulations, as discussed in the section 6, do include the complete interaction of the laser pulse with all states in the molecule.

For later discussions we define the states $4^1\Sigma_n^+$ and $2^1\Pi_g$ as the *lower target channel* and the states $5^1\Sigma_g^+$, $6^1\Sigma_g^+$ and $3^1\Pi_g$ as the *upper target channel*. The control objective is to design laser pulse shapes which selectively populate only one of these target channels. In the experiment the target state populations are measured by post-ionization with a probe pulse of a different wavelength and extracted from the energy-resolved detection of photoelectrons (PEs) released from the target states.

4. Experimental setup

The experimental setup is depicted in figure 3. An amplified Ti:Sapphire laser system provides pulses with an intensity FWHM of 25 fs, a central wavelength of 795 nm and a maximum pulse energy of 0.8 mJ at a repetition rate of 1 kHz. The pulses pass a beamsplitter and one third of the energy of the beam enters our home-built LC-SLM based pulse shaper [34]. The pulses are then steered via a polarization rotating periscope (P) and a variable ND attenuator (A) and are focused by an $f = 30$ cm lens (L) into the interaction region of a magnetic bottle time-of-flight spectrometer. The remaining two thirds of the laser beam are used to pump an OPA (optical parametric amplifier) to generate the probe pulse at 570 nm. This wavelength provides maximum visibility of the PEs from the molecular target states. The BWL OPA pulse

molecules in the beam by the IR-control pulse and the visible probe pulse only is subtracted. The spectrometer resolution is not sufficient to disentangle the signals from the individual states directly. To evaluate the contributions of the upper and the lower target channel from the overlapping PE spectra the signals are fitted with Gaussian functions for every state using a Levenberg–Marquard-algorithm. The lower bound of the peak width is given by the spectrometer resolution of 70 meV at 1 eV PE energy. From these fits the contrast according to (3) of each spectrum is determined.

6. Simulations

To model the strong-field interaction of shaped fs laser pulses with K_2 molecules we solve the time-dependent-Schrödinger-equation numerically employing a grid-based split-operator-technique. The Hamiltonian of the system interacting with the control field in the length-gauge \hat{H}_0 is given by

$$\hat{H}_0(t, R, \theta) = \mathcal{T} + \mathcal{V}_0(R) + \mathcal{W}_0(t, R, \theta)$$

$$\mathcal{T} = -\frac{\hbar^2}{2\mu} \frac{\partial^2}{\partial R^2} \hat{\mathbf{1}}$$

$$\mathcal{V}_0(R) = \begin{pmatrix} V_X(R) & 0 & 0 & 0 & 0 & 0 & 0 & 0 \\ 0 & V_A(R) - \hbar\omega_0 & 0 & 0 & 0 & 0 & 0 & 0 \\ 0 & 0 & V_{4\Sigma}(R) - 2\hbar\omega_0 & 0 & 0 & 0 & 0 & 0 \\ 0 & 0 & 0 & V_{2\Pi}(R) - 2\hbar\omega_0 & 0 & 0 & 0 & 0 \\ 0 & 0 & 0 & 0 & V_{5\Sigma}(R) - 2\hbar\omega_0 & 0 & 0 & 0 \\ 0 & 0 & 0 & 0 & 0 & V_{6\Sigma}(R) - 2\hbar\omega_0 & 0 & 0 \\ 0 & 0 & 0 & 0 & 0 & 0 & V_{3\Pi}(R) - 2\hbar\omega_0 & 0 \end{pmatrix}$$

$$\mathcal{W}_0(t, R, \theta) = -\frac{\hbar}{2} \begin{pmatrix} 0 & \Omega_{XA}^+(t, R, \theta) & 0 & 0 & 0 & 0 & 0 & 0 \\ \Omega_{XA}^-(t, R, \theta) & 0 & \Omega_{A4\Sigma}^+(t, R, \theta) & \Omega_{A2\Pi}^+(t, R, \theta) & \Omega_{A5\Sigma}^+(t, R, \theta) & \Omega_{A6\Sigma}^+(t, R, \theta) & \Omega_{A3\Pi}^+(t, R, \theta) & \\ 0 & \Omega_{A4\Sigma}^-(t, R, \theta) & 0 & 0 & 0 & 0 & 0 & \\ 0 & \Omega_{A2\Pi}^-(t, R, \theta) & 0 & 0 & 0 & 0 & 0 & \\ 0 & \Omega_{A5\Sigma}^-(t, R, \theta) & 0 & 0 & 0 & 0 & 0 & \\ 0 & \Omega_{A6\Sigma}^-(t, R, \theta) & 0 & 0 & 0 & 0 & 0 & \\ 0 & \Omega_{A3\Pi}^-(t, R, \theta) & 0 & 0 & 0 & 0 & 0 & \end{pmatrix} \quad (4)$$

The elements of \mathcal{V}_0 are the R-dependent potential energies. Because all transitions involved are almost resonant, we use the rotating-wave-approximation (RWA) to describe the laser-induced coupling between the molecular states. These couplings are the elements of \mathcal{W}_0 and they are given in terms of the Rabi-frequencies

$$\Omega_{MN}^-(t, R) = \vec{\mu}_{MN}(R) \cdot \vec{\mathcal{E}}^-(t)/\hbar = (\Omega_{MN}^+(t, R))^* \quad (5)$$

Here $\vec{\mathcal{E}}^-(t)$ describes the complex envelope of the (negative frequency) electric field. All target states are coupled to the $A^1\Sigma_u^+$ state but the transitions are driven by different polarization components of the electric field [8]. The parallel transitions ($\Sigma \rightarrow \Sigma$) interact with the parallel component of the electric field $\mathcal{E}^-(t) \cos(\theta)$ and the transitions $\Sigma \rightarrow \Pi$ are driven by the perpendicular component of the field $\mathcal{E}^-(t) \sin(\theta)$, where θ is the angle between the molecular axis and the driving laser-field. This results in the following couplings:

$$\begin{aligned} \hbar\Omega_{XA}^-(t, R, \theta) &= \mu_{XA}(R)\mathcal{E}^-(t) \cos(\theta) \\ \hbar\Omega_{A4\Sigma}^-(t, R, \theta) &= \mu_{A4\Sigma}(R)\mathcal{E}^-(t) \cos(\theta) \end{aligned}$$

$$\begin{aligned} \hbar\Omega_{A2\Pi}^-(t, R, \theta) &= \mu_{A2\Pi}(R)\mathcal{E}^-(t) \sin(\theta) \\ \hbar\Omega_{A5\Sigma}^-(t, R, \theta) &= \mu_{A5\Sigma}(R)\mathcal{E}^-(t) \cos(\theta) \\ \hbar\Omega_{A6\Sigma}^-(t, R, \theta) &= \mu_{A6\Sigma}(R)\mathcal{E}^-(t) \cos(\theta) \\ \hbar\Omega_{A3\Pi}^-(t, R, \theta) &= \mu_{A3\Pi}(R)\mathcal{E}^-(t) \sin(\theta). \end{aligned} \quad (6)$$

The R-dependent PES and dipole-moments can be seen in figure 2. In the simulations the contrast value achieved by a certain laser pulse shape is calculated from the final populations c^2 in the target channels. They are computed as

$$\begin{aligned} c_{\text{upper}}^2(\infty) &= |c_{5\Sigma}(\infty)|^2 + |c_{6\Sigma}(\infty)|^2 + |c_{3\Pi}(\infty)|^2 \\ c_{\text{lower}}^2(\infty) &= |c_{4\Sigma}(\infty)|^2 + |c_{2\Pi}(\infty)|^2 \end{aligned} \quad (7)$$

in accordance with the definition of the target channels in section 3.

The description of strong-field effects requires the consideration of intensity averages in the interaction region to achieve a more realistic description of our experiment. The volume or intensity averaging describes the inherent averaging over the intensity distribution in the focus of the IR-pulse by the probe pulse. The averaged excitation $\langle \mathcal{S} \rangle$ that is reached inside a certain intensity distribution $I(r, z)$ is given by weighting the excitation for a given intensity $\mathcal{S}(I)$ with the differential volume with this intensity $dV = f(I) dI$

$$\langle \mathcal{S} \rangle = \frac{\int_{I_{\min}}^{I_0} f(I)\mathcal{S}(I) dI}{\int_{I_{\min}}^{I_0} f(I) dI} \quad (8)$$

The expression for $f(I)$ is found starting from the spatial intensity distribution of a focused Gaussian beam with a maximum intensity I_0 at $(r, z) = (0, 0)$, a Rayleigh-range z_R and a beam-waist of w_0 [35]

$$I(r, z) = I_0 \frac{1}{1 + \left(\frac{z}{z_R}\right)^2} \exp\left[-\frac{2r^2}{w_0^2 \left\{1 + \left(\frac{z}{z_R}\right)^2\right\}}\right] \quad (9)$$

The volume of the rotational ellipsoid, that contains all intensities higher than I is given by

$$V(I) = 2\pi \int_0^{z_R \sqrt{\frac{I_0}{I} - 1}} r^2(I, z) I(z) dz \quad (10)$$

with

$$r^2(I, z) = -\frac{w_0}{2} \left(1 + \frac{z^2}{z_R^2}\right) \ln \left[\frac{I}{I_0} \left(1 + \frac{z^2}{z_R^2}\right) \right]. \quad (11)$$

The volume containing the intensities $[I, I + dI]$ is given by $\frac{\partial V}{\partial I} dI$. Hence the derivative of (10) with respect to I gives the sought-for distribution function $f(I)$

$$\frac{\partial V(I)}{\partial I} = f(I) = \frac{\pi w_0^2 z_R (2I + I_0)}{3I^2} \sqrt{\frac{I_0}{I} - 1}. \quad (12)$$

The averaged excitations converge for eight gridpoints of the distribution function of the intensity. A minimum intensity of $I_{\min} = 0.05I_0$ proves to be sufficient, as there is no significant excitation into the target channels at so low an intensity.

In addition, in the experiments the molecules are not aligned before the excitation. Consequently their random orientation with respect to the polarization of the driving laser field has to be taken into account when calculating the population dynamics. Especially as the intra-molecular transitions to the target states are driven by different components of the electric field (parallel or perpendicular to the internuclear axis) it is crucial to consider these orientations, cf (6). The averaged excitation obtained for a given distribution of orientations $f(\theta, \phi)$ is given by

$$\begin{aligned} \langle \mathcal{S} \rangle &= \frac{\int_0^{2\pi} \int_0^\pi f(\theta, \phi) \mathcal{S}(\theta) \sin(\theta) d\theta d\phi}{\int_0^{2\pi} \int_0^\pi f(\theta, \phi) \sin(\theta) d\theta d\phi} \\ &= 2 \int_0^{2\pi} \int_0^{\pi/2} f(\theta, \phi) \mathcal{S}(\theta) \sin(\theta) d\theta d\phi. \end{aligned} \quad (13)$$

Again θ is the angle between molecular axis and laser polarization, and ϕ is a polar angle which does not influence the interaction. Comparison of simulations and experimental data suggests that the best agreement is obtained under the assumption of an isotropic distribution $f_{iso}(\theta, \phi) = \frac{1}{4\pi}$ of molecular orientations. Also here eight sampling points for the angular distribution function are sufficient to ensure a convergence of the simulated excitations. In practice we calculate the quantum dynamics at a given intensity for the different molecular orientations and subsequently perform the intensity averaging. A simulated contrast landscape, that includes volume and orientation averaging, is shown in figure 5. Still the exact features of the landscape are extremely sensitive to experimental circumstances like the particular intensity distribution in the laser focus or the spatial overlap between the control and the probe pulse.

For a transparent analysis we will discuss the control mechanism for the case of a molecule fixed in space at $\theta = 45^\circ$ with respect to the driving laser field at a single intensity, the maximum intensity I_0 that is reached in the centre of the laser focus. In view of the proposed control scenario it is of particular interest to investigate the phase relation of the induced dipole-moment in the $X^1\Sigma_g^+ - A^1\Sigma_u^+$ system and the electric field of the

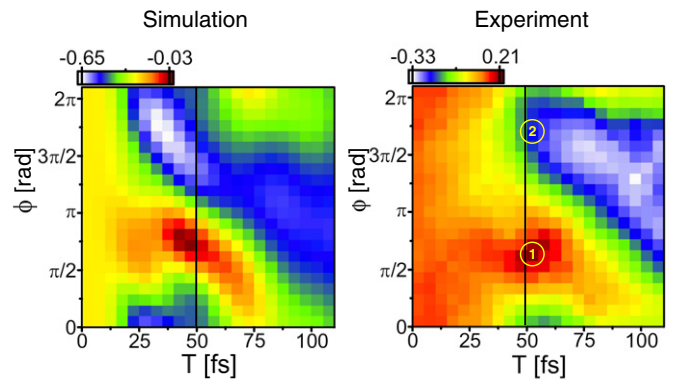


Figure 5. Comparison between a simulated contrast landscape (left), including the averages over intensity distribution and molecular orientation and the measured contrast landscape (right). The experimental landscape was recorded using 795 nm control pulses with BWL-FWHM of 25 fs and a peak intensity of $8.5 \times 10^{11} \text{ W cm}^{-2}$. The points ① and ② are highlighted for later discussions.

laser pulse. The time-dependent dipole-moment is calculated according to

$$\langle \mu_{XA} \rangle(t) = \int_0^\infty \mu_{XA}(R) \cdot \{ \psi_X^*(R, t) \psi_A(R, t) e^{-i\omega_0 t} + \text{c.c.} \} dR \quad (14)$$

where $\psi_X(R, t)$ and $\psi_A(R, t)$ are the nuclear wavefunctions in the $X^1\Sigma_g^+$ and $A^1\Sigma_u^+$ state in their spatial representations⁵. During the interaction with the driving laser field the vibronic wavepackets propagate on the PES, resulting in a time-dependent expectation value of the internuclear separation $\langle R(t) \rangle = \int_0^\infty |\psi(R)|^2 R dR$. In accordance with the calculation of $\langle \mu_{XA} \rangle(t)$ in the $X^1\Sigma_g^+ - A^1\Sigma_u^+$ system also here the expectation value of the internuclear separation $\langle R(t) \rangle$ is calculated within the subsystem consisting of these states. As the wavepackets stay rather localized during the interaction with the laser pulse the analysis of the single parameter proves sufficient and allows for a transparent physical picture. The time-dependence of $\langle R(t) \rangle$ leads to a time-dependent change of the frequency and the phase of the dipole-oscillation due to the changing energy-difference between the $X^1\Sigma_g^+$ state and the $A^1\Sigma_u^+$ state at $\langle R(t) \rangle$. The crucial influence of vibrational wavepacket dynamics onto the control scenario and the consequences for the phase-evolution with respect to the electric field were confirmed by simulations that disregarded the kinetic operator \mathcal{T} , cf (4). These simulations did not include propagation of the wavepackets on the PES and therefore no associated phase dynamics or changes in the resonance frequency of the electronic charge oscillation did occur. Although the described scenario particularly depends on the in-phase and out-of-phase oscillations of the electric field and the induced dipole-moment it is sufficient to calculate the simulations in the framework of the RWA because the phase of the driving laser field, vital to the control scenario, is contained in the complex envelope of the electric field.

In our simulations we assume the ionization process to be perturbative, i.e. it does not alter the populations in the

⁵ Supplementary material to [25].

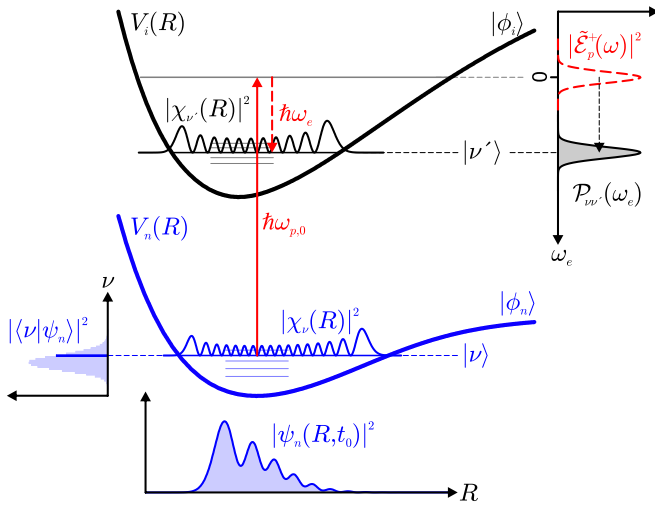


Figure 6. Construction of the partial PE spectrum arising from a specific vibronic transition $|\nu\rangle \rightarrow |\nu'\rangle$. The wavefunction $\psi_n(R, t_0)$ in the electronic molecular state $|\phi_n\rangle$ (blue potential) is decomposed into the vibrational eigenfunctions. Ionization can occur from a vibrational eigenstate $|\nu\rangle$ of $V_n(R)$ into any vibrational eigenstates $|\nu'\rangle$ of the ionic state $|\phi_i\rangle$ (black potential) for which the energy-difference between $|\nu\rangle$ and $|\nu'\rangle$ is equal or less than the energy of the absorbed photon $\hbar\omega_{p,0}$. The difference in energy (red dashed arrow) will be carried away by the emitted electron as kinetic energy.

neutral molecular (and atomic) states. For comparison with the measurements the PE signals, as seen for example in figure 4, are calculated based on the quantum mechanical population dynamics simulations, that include volume and orientation averaging, in the following way: We consider the diatomic molecule in a previously excited neutral electronic state $|\phi_n\rangle$. Let $V_n(R)$ be the electronic potential of this state as a function of the internuclear distance R . Now the excited molecule is ionized by a weak probe pulse, whose spectrum $\tilde{\mathcal{E}}_p^+(\omega)$ is centred around a frequency $\omega_{p,0}$ which is sufficiently large to induce a one-photon transition to an ionic state $|\phi_i\rangle$ (cf figure 6). Since the probe pulse is weak the ionization process is treated perturbatively. To this end we expand the nuclear wave function $\psi_n(R, t_0)$ in the neutral state at time t_0 prior to the ionization (but after the interaction with the control pulse) as

$$\psi_n(R, t_0) = \sum_{\nu=0}^{\infty} \langle \nu | \psi_n \rangle \chi_{\nu}(R). \quad (15)$$

The $\chi_{\nu}(R)$ are the vibrational eigenfunctions of the potential $V_n(R)$ corresponding to eigenstates $|\nu\rangle$ and eigenenergies $\hbar\omega_{\nu}$. The absolute squares $|\langle \nu | \psi_n \rangle|^2$ describe the population distribution among the vibrational states $|\nu\rangle$ after excitation. Now consider a given vibrational state ν and a fixed frequency ω_p out of the probe spectrum. Starting from $|\nu\rangle$ this frequency component may induce transitions to any vibrational state $|\nu'\rangle$ of the ionic potential $V_i(R)$, whose energy $\hbar\omega_{\nu'}$ is smaller or equal to $\hbar\omega_{\nu} + \hbar\omega_p$. The difference energy $\hbar\omega_e = \hbar(\omega_{\nu} + \omega_p - \omega_{\nu'})$ will be carried away by the ejected PE in form of kinetic energy. In the framework of time-dependent perturbation theory the probability $\mathcal{P}_{\nu\nu'}$ for such a transition is proportional to the population of the initial state $|\nu\rangle$, the

overlap of the nuclear wavefunctions given by the Franck–Condon factor $|\langle \nu' | \nu \rangle|^2$, and the spectral intensity of the probe pulse at $\omega_p = \omega_p(\omega_e)$:

$$\mathcal{P}_{\nu\nu'}(\omega_e) \propto |\langle \nu | \psi_n \rangle|^2 \cdot |\langle \nu' | \nu \rangle|^2 \cdot |\tilde{\mathcal{E}}_p^+(\omega_p)|^2. \quad (16)$$

The total PE spectrum as a function of the kinetic excess energy $\hbar\omega_e$ is obtained by summation of this expression over all ν , and for every ν over all ν' for which $\omega_e \geq 0$:

$$\mathcal{P}(\omega_e) \propto \sum_{\nu, \nu': \omega_e \geq 0} \left| \langle \nu | \psi_n \rangle \langle \nu' | \nu \rangle \tilde{\mathcal{E}}_p^+(\omega_e + \omega_{\nu'} - \omega_{\nu}) \right|^2. \quad (17)$$

Alternatively the PE spectra are calculated based on Mulliken’s semi-classical difference potential analysis [36–38]. This analysis has the additional advantage of giving an intuitive understanding of the shape of the PE signals produced from the molecular states. Figure 10 shows the nuclear dynamics after excitation of the $5^1\Sigma_g^+$ and of the $2^1\Pi_g$ state. The mapping of the changing internuclear separation onto the difference potential directly translates into the distribution of kinetic energies in the PE spectrum. The results of both approaches are in excellent agreement with the measured PE spectra.

7. Experimental results

In the experiments we study intensity and phase control for the selective population of the upper and the lower target channel in the potassium dimer. First we demonstrate the non-perturbative character of the excitation by investigating the intensity dependence of the PE spectra after interaction with a BWL IR-pulse. These measurements serve to rule out higher order spectral interference as the key mechanism of changes in the PE spectrum. In the second part of the experiment, the intensity $I_0 = 8.5 \times 10^{11} \text{ W cm}^{-2}$ was chosen and the spectral phase was varied. In particular, we investigated the variation of the contrast as a function of the sine-phase ϕ and the sine-frequency T in the spectral phase function defined in (2).

7.1. Intensity dependence

Two-colour PE spectra resulting from the excitation of K_2 with BWL pump pulses of various pulse energies are shown on the right side of figure 4. Upon weak-field excitation (spectrum of the lowest pulse energy of less than $0.1 \mu\text{J}$), only the $2^1\Pi_g$ state is excited (cf figure 2), giving rise to a double-peak contribution in the spectrum around $E_{\text{kin}} = 1 \text{ eV}$. The two humps in the $2^1\Pi_g$ signal structure are related to ionization of the vibrating molecule at the inner and outer turning point. In analogy to a classical vibration, the probability of finding the nuclear wavepacket is highest at the two turning points [39, 40]. Because the difference potential $\Delta V(R) = V_{\text{ionic}}(R) - V_{2^1\Pi}(R)$ is quite steep (cf also figure 10), both turning points are mapped onto different kinetic energies and are hence clearly discerned in the PE spectrum. The contrast of $C = -0.3$ instead of a perfect $C = -1$ can be explained by background signals hampering the evaluation. With increasing intensity, however, the energy-splitting in the resonant $X^1\Sigma_g^+ - A^1\Sigma_u^+$ subsystem grows and the upper target channel becomes accessible as well. As a result, at pulse energies above $0.1 \mu\text{J}$ an additional

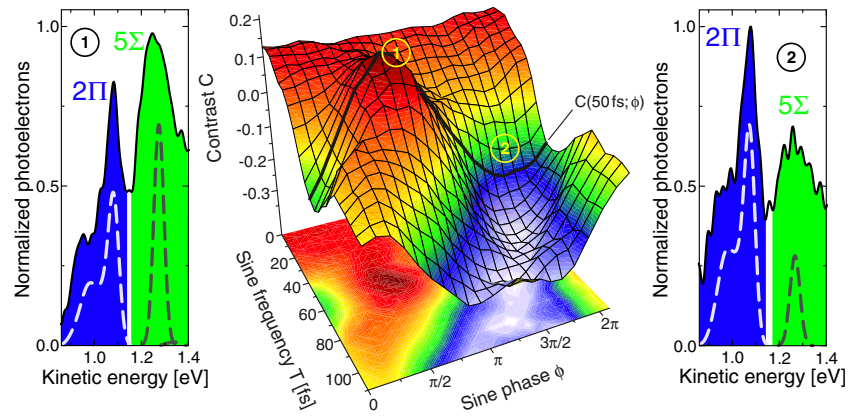


Figure 7. Contrast landscape for the systematic variation of T and ϕ . Every point of the landscape corresponds to a specific PE spectrum, with the according contrast value $C(T, \phi)$ encoded in the colour and the height. A clear maximum, marked ① in the landscape, emerges around $T = 50$ fs and $\phi_1 = 1.8$ rad. A change of ϕ by ca π leads to a point ϕ_2 where the contrast is significantly reduced, ②. The measured PE spectra, that correspond to the points ① and ② are also shown along with simulated PEs (dashed lines) to the left ① and the right ② side of the landscape.

peak shows up in the spectrum at $E_{\text{kin}} = 1.25$ eV. This peak is attributed to population of the $5^1\Sigma_g^+$ state. The related difference potential is almost flat, therefore the two turning points are mapped onto the same kinetic energy in this case so that the $5^1\Sigma_g^+$ signal shows up as one localized peak. Once the $5^1\Sigma_g^+$ state can be populated its signal dominates the spectrum and the contrast starts to increase up to $C = 0.12$ for I_0 at a pulse energy of $0.3\mu\text{J}$. The explanation for the observation, that even the BWL pulse switches the population between the target states, is related to the off-resonance of the central wavelength of our laser spectrum. Due to a slight *blue*-shift of the laser central wavelength (at 795 nm) with respect to the $X^1\Sigma_g^+ - A^1\Sigma_u^+$ resonance at 830 nm (around $R_0 = 3.9$ Å) field and dipole already oscillate almost out-of-phase upon creation of the dipole. Therefore the excitation is biased towards population of the upper LIP and consequently towards the upper target channel once the latter becomes energetically accessible (green contribution to the spectra at higher pulse energies). Laser pulses at the exact resonance frequency are expected to perform even better in terms of selectivity to both directions. Experiments with an optimized spectrum are currently being carried out. As all PE spectra were acquired by laser pulses with the same spectral amplitude and phase, these results verify that the appearance of signal from the upper target channel is a genuine strong-field effect and cannot be explained by the weak-field control scenarios of spectral interference.

For the phase-control experiments the pulse energy of $0.3\mu\text{J}$ was chosen because at this pulse energy the BWL pulse addresses both target channels and adjacent background signals from direct ionization are yet negligible (cf red and yellow line in the spectrum). The corresponding spectrum is marked in red on the right side of figure 4. The same PE spectrum is shown on the left side of the figure. The simulated signals, calculated based on the description in section 6 are in excellent agreement with the measured ones, including the atomic signal resulting from one-photon-ionization of the potassium 4p state by the probe pulse.

7.2. Phase control

In section 6 we have shown that the relative phase of the molecular dipole and the laser field controls the interaction energy. Therefore, we investigate control exerted by the relative temporal phase by manipulation of the spectral phase of the laser pulse. Control over this temporal phase is achieved by sinusoidal spectral phase modulation (according to (2)). From coarse scans we found that at an amplitude of $A = 0.8$ a high degree of control over both target channels is observed. At this sine-amplitude we varied the parameters T and ϕ and recorded spectra for a contrast landscape [22], that is shown in figure 7. For $T = 0$ fs the phase modulation (2) only introduces a constant phase which does not affect the control process. Therefore the corresponding line in the landscape shows the contrast as achieved by the BWL-pulse. The use of actually shaped pulses creates a rich topology, with a marked maximum for the parameters $T = 50$ fs and $\phi = 1.8$ rad, point ① in figure 7. The PE spectrum with the contrast value of $C = 0.21$ can be seen on the left side of figure 7. The yield from the upper target channel clearly exceeds the yield from the lower target channel indicating selective population of the $5^1\Sigma_g^+$ state. Also the yield from the higher target channel that is reached by excitation with the BWL-pulse (cf figure 4) is surpassed by the shaped laser-field. In the spirit of earlier SPODS-experiments [12] we follow the line of constant T on the landscape and arrive at a point around $\phi_2 = \phi_1 + \pi$ of inverted contrast $C = -0.2$, point ② in figure 7. From the PE spectrum behind this landscape point on the right side of figure 7 we see, that PEs from the lower target channel dominate the spectrum, while only little signal from the upper target channel was detected. As seen in figure 5 the simulation reproduces the measured contrast landscape well. For the discussion of the control mechanism behind the distinct points ① and ② in the next section we refer to these calculations. The global minimum of the landscape is found at higher T .

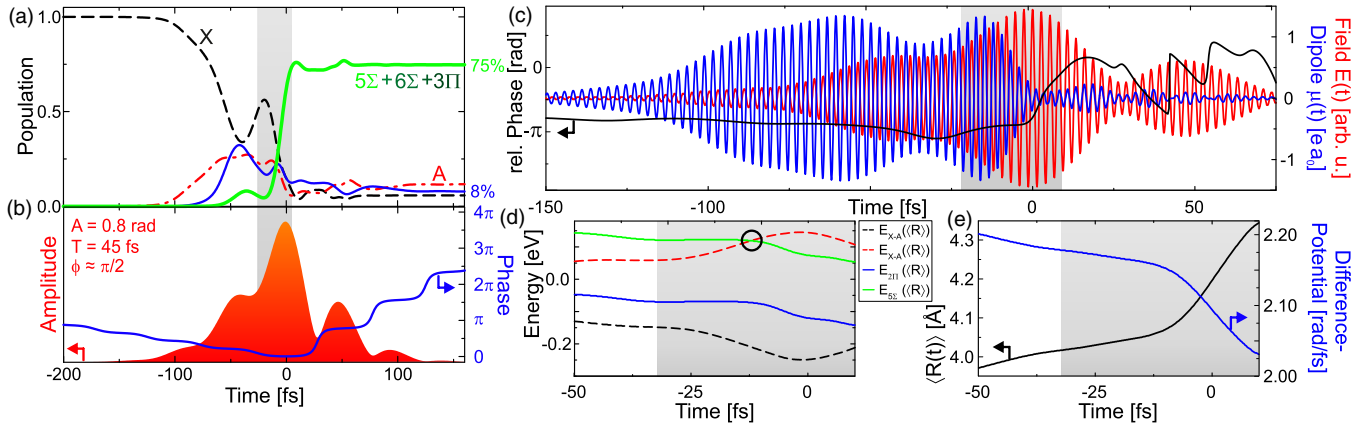


Figure 8. Dynamics of the population of the upper target channel. (a) Simulated population dynamics for the control pulse depicted in (b). The bright green line is the population accumulated in the upper target channel. The shaped electric field is decomposed into its envelope (red background) and temporal phase (blue line). (c) Oscillations of the electric field (red) and the induced dipole-moment in the $X^1\Sigma_g^+-A^1\Sigma_u^+$ system (blue). The slowly varying black line is the relative phase of the oscillations of the dipole-moment and the electric field. (d) Energy of the LIPs in the $X^1\Sigma_g^+-A^1\Sigma_u^+$ subsystem (black and red) and of the $5^1\Sigma_g^+$ (green) and the $2^1\Pi_g$ (blue) state at $\langle R(t) \rangle$ shifted by two photon energies $\hbar\omega_0$. (e) Temporal evolution of the expectation value of the internuclear separation (black) and the corresponding value of the difference potential between the $X^1\Sigma_g^+$ and the $A^1\Sigma_u^+$ state of K_2 (blue). The grey-shaded background marks the decisive time-window of the final population transfer in all frames.

8. Physical mechanism

In this section we illuminate the physical mechanism that allows us to selectively populate one of the molecular target channels using shaped femtosecond laser pulses. To this end we analyse the quantum mechanical simulations as described in section 6. The physical mechanism is revealed by inspection of the calculated neutral population dynamics induced by the shaped laser field. Figure 8 shows the population dynamics for point ① in figure 7. Initially around $t = -50$ fs, the potassium dimer is steered into a coherent superposition of the $X^1\Sigma_g^+$ and the $A^1\Sigma_u^+$ state, i.e. a coherent charge oscillation is formed, cf frame (a). As the central wavelength of the laser pulse is blue detuned with respect to the $X^1\Sigma_g^+-A^1\Sigma_u^+$ resonance the induced oscillation follows the driving laser field with a phase difference of π , as can be seen in frame (c) from the oscillations and more directly from the relative phase. However during the ensuing interaction with the laser pulse the electronic coherence is influenced by vibrational wavepacket dynamics. Frame (e) shows the expectation value of the internuclear separation $\langle R(t) \rangle$ in the $X^1\Sigma_g^+-A^1\Sigma_u^+$ system (black). The wavepacket starts at the equilibrium distance of $R = 3.9$ Å. $\langle R(t) \rangle$ then increases due to the wavepacket propagation on the PES. The blue line represents the difference potential between the $X^1\Sigma_g^+$ and the $A^1\Sigma_u^+$ state that is proportional to the oscillation frequency at $\langle R(t) \rangle$. This frequency decreases in accordance with the decreasing difference potential. Due to the change in frequency also the phase relation between charge oscillation and laser field is changed and the condition of out-of-phase oscillation for maximizing the interaction energy is no longer fulfilled. Due to the spectral shaping of the laser pulse, leading to a time-varying phase of the electric field (blue line in frame (b)) the desired phase relation is maintained. The most intense part of the laser pulse around $t = 0$ fs energetically opens up the upper target channel, cf frame (d).

At these intensities the induced splitting of the LIPs in the $X^1\Sigma_g^+-A^1\Sigma_u^+$ system, indicated by the red and black dashed lines, is sufficient to shift the upper LIP (red) into resonance with the energy of the $5^1\Sigma_g^+$ state (green line), as marked by the black circle. By virtue of the maximized interaction energy the population is steered into the upper target channel. Although the lower target channel, specifically the $2^1\Pi_g$ state (blue line in frame (d)) could be reached during the whole interaction, the phase relation between electric field and induced charge oscillation prevents an efficient population transfer. A detailed analysis of the vibrational wavepacket dynamics reveals that between the built-up of the coherence at $t = -50$ fs and the transfer of the population to the upper target channel the internuclear distance increases by 9% entailing a change of the Bohr-frequency in the $X^1\Sigma_g^+-A^1\Sigma_u^+$ system of 110 meV, which corresponds to a wavelength change of 70 nm.

The simulated population dynamics corresponding to point ② are shown in figure 9. The system is also led into a coherent superposition of the $X^1\Sigma_g^+$ and the $A^1\Sigma_u^+$ state, as seen in frame (a) around $t = -50$ fs. After some Rabi-type oscillations the population is finally transferred to the lower target channel, the time-window for the switching being highlighted by a grey background. The coherent population return during the pulse is due to the stronger coupling of the $A^1\Sigma_u^+$ state to the lower target channel in comparison to the upper target channel, cf figure 2. The oscillation of the time-dependent dipole-moment with respect to the shaped electric field, cf frame (c) in figure 9, reveals that the final population transfer to the lower target channel at $t = 50$ fs is indeed due to in-phase-oscillation and a resulting minimization of the interaction energy. Despite the blue-detuning of the laser central frequency, which promotes an out-of-phase oscillation, the electric field was shaped to ensure the required phase relation during the time-window of excitation. At earlier times during the interaction around $t = -50$ fs the two quantities

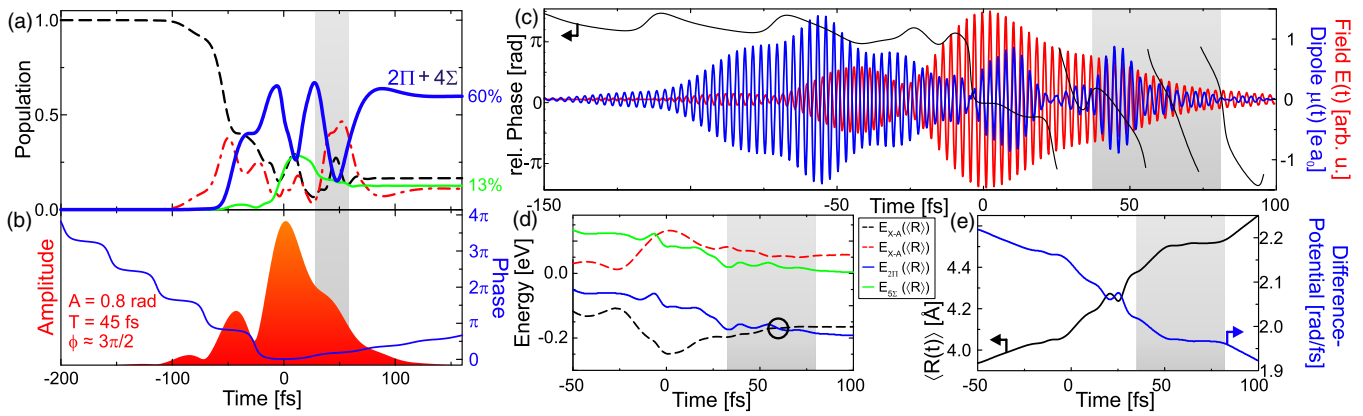


Figure 9. Same as figure 8 for the population of the lower target channel.

oscillate out-of-phase. However during this time the upper target channel cannot be reached as the induced energetic splitting of the LIPs is not yet high enough. Frame (d) shows this splitting in the $X^1\Sigma_g^+-A^1\Sigma_u^+$ system together with the energies of the $5^1\Sigma_g^+$ (green line) and the $2^1\Pi_g$ (blue line) state at $\langle R(t) \rangle$. For these early times the upper target channel cannot be reached from the upper LIP (red line) therefore no population transfer occurs. During the most intense part of the pulse around $t = 0$ fs the upper target channel would be accessible. By virtue of the shaping electric field and dipole oscillate in phase during this time. Hence no population is transferred to the upper target channel. Instead at slightly later times around $t = 50$ fs the energy of the $2^1\Pi_g$ state shifts into resonance with the lower LIP of the $X^1\Sigma_g^+-A^1\Sigma_u^+$ system (black, dashed line) at the current internuclear separation, as marked by the black circle. It is the lower LIP that is populated, due to the in-phase oscillation of field and dipole (cf grey-shaded time-window in frame (c)) and the population flows into the lower target channel. In general the phase dynamics are less smooth than in case ①. Despite the steps in the temporal phase of the electric field the dipole readily returns to the out-of-phase oscillation, as seen until around $t = 0$ fs. At this time the field is strong enough to force the dipole into the required in-phase oscillations. An analysis of the quantum dynamics at lower intensities reveals that it is indeed a genuine strong-field effect that forces the dipole to oscillate in-phase with the electric field. For lower intensities the phase dynamics gradually change into a constant phase difference of π as determined by the blue-detuning of the driving field. Still the excitation will result in population of the lower target channel as the energetic splitting in the $X^1\Sigma_g^+-A^1\Sigma_u^+$ system is insufficient to reach the upper target channel. The interaction time of the molecule with the laser pulse between the built-up of the coherent superposition, i.e. the charge oscillation, around $t = -50$ fs and the final population transfer at $t = 50$ fs is longer than in the case of point ①. The nuclear dynamics during this time entail a larger change in the internuclear separation, black line in frame (e). Also they prove to be more complex than in the first case and $\langle R(t) \rangle$ shows a more structured behaviour. The Bohr-frequency decreases by $190 \text{ meV} \hat{=} 130 \text{ nm}$ as the internuclear distance is changed by 18%.

The movies in the supplementary material (available from stacks.iop.org/JPhysB/47/124015/mmedia) show the complete electron dynamics during the excitations with the fields of point ① and ②. They illustrate how the stationary ground state distribution of the $X^1\Sigma_g^+$ state is shaken into a superposition with the $A^1\Sigma_u^+$ state by the field. To reach the target state also the higher lying electronic states contribute to the electron density at later times of the light field. Finally the molecule resides in one of the target channels, that comprise specific three-dimensional electron densities. The oscillation of the whole electron distribution with respect to the field during the interaction once again exemplifies the discussed phase relations for the two distinct cases. Also shown are the time evolution of the population in the contributing electronic states during the interaction with the light field as well as the amplitude and the relative phase between the electric field of the light pulse and of the oscillating charge distribution. For details of the computation see footnote 5.

The global minimum of the contrast landscape in figure 7 occurs at larger sine-frequencies T . An analysis of quantum dynamics for large T shows, that the dipole-moment in the $X^1\Sigma_g^+-A^1\Sigma_u^+$ system induced by one subpulse vanishes before the next excitation takes place. Due to the increasing temporal separation of the subpulses the wavepacket created in the $A^1\Sigma_u^+$ state has time to propagate far enough for the wavefunction-overlap (cf (14)) to decrease to zero. No oscillating dipole-moment remains and an interpretation of the quantum dynamics and the acquired target channel population in terms of the discussed control mechanism is therefore not applicable. It is rather a matter of successive population of the lower target channel by each subpulse after the wavepacket in the $A^1\Sigma_u^+$ state has moved out of the Franck-Condon-window.

In order to exemplify that by selective excitation of specific molecular states different temporal nuclear dynamics are induced in the molecule figure 10 shows the ensuing nuclear dynamics in the states $5^1\Sigma_g^+$ (left) and $2^1\Pi_g$ (right) after excitation with the discussed control fields. The different roundtrip-times for the wavepacket can clearly be seen along with the different ranges of internuclear separations that are covered. Together with the difference potentials of the ionic

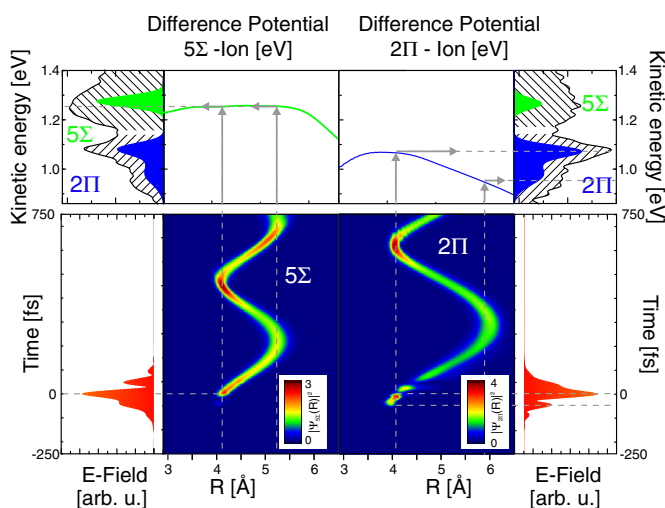


Figure 10. Wave packet dynamics in the states $5^1\Sigma_g^+$ (left) and $2^1\Pi_g$ (right) during and after the excitation with the control pulses as seen in figures 8 and 9. Also shown are the difference potentials of the ionic PES and the respective state. They visualize why the signals from the $5^1\Sigma_g^+$ state (left) and $2^1\Pi_g$ state (right) differ significantly in shape, as seen from the PE signals. In these the measured signals are indicated as hatched areas, the coloured peaks are calculated signals.

molecular state and the $5^1\Sigma_g^+$ state, respectively the $2^1\Pi_g$ state, these nuclear dynamics rationalize the shape of the associated measured (hatched areas) and simulated (filled areas) PE signals.

9. Conclusions

We have shown experimentally that the specific shaping of the temporal amplitude and phase of an ultrashort laser pulse enables efficient control of the interplay between induced charge oscillation and the driving field. Control of the coupled electron-nuclear wavepacket dynamics was achieved by adapting the phase relation between field and dipole in order to selectively populate LIPs in the driven system by minimizing or maximizing the interaction energy. A deeper analysis of the quantum mechanical simulations reveals the delicate interplay between the oscillating charge distribution and the control field. Especially the nuclear dynamics and their influence onto the electronic resonance prove to be an important factor in this regard. In addition the temporal intensity distribution of the driving field, i.e. the amplitude of the field, is essential to induce energetic splittings and level shifts, that also depend on the wavepacket propagation. Moreover, for the reproduction of the experimental findings, orientation averaging and averaging over the focal intensity distribution turn out to be indispensable. In conclusion tailoring the intricate interplay between driving laser field and induced dipole-moment results in a modulation of the relative phase and the energetic splitting and provide an avenue to steer the system selectively into bespoke target channels, that may even be completely inaccessible in the case of weak-field excitation.

In ongoing experiments with K_2 we explore the recurrence of the electronic coherence in the $X^1\Sigma_g^+-A^1\Sigma_u^+$ subsystem around 500 fs after the first excitation by using interferometric double pulses for selective excitation. Simulations indicate that the dipole-moment is even stronger at this point of the temporal evolution and would enable an even higher degree of control over the populations in the target channels [33]. Additionally first experimental evidence shows that femtosecond laser pulses that are shaped with spectral phases consisting of second and third order polynomial modulation [42] offer a high degree of control over the populations in selected electronic states of the potassium dimer.

Additionally first hints as to the same control mechanism being at work also in larger systems were found in experiments on isopropyl alcohol. Sinusoidally phase shaped femtosecond laser pulses were used to trigger a controlled fragmentation of the molecules [41]. We observed a clear modulation of the ion yield in dependence on the sine-parameter ϕ , that could not be attributed to effects like intensity variations. Therefore we think that the devised scheme is universal and has promise for applications ranging from control in complex systems to quantum information processing [43].

Acknowledgments

We thank the Deutsche Forschungsgemeinschaft for the financial support.

References

- [1] Shapiro M and Brumer P 2011 *Quantum Control of Molecular Processes* (Berlin: Wiley) and references therein
- [2] Zewail A 2000 Femtochemistry: atomic-scale dynamics of the chemical bond *J. Phys. Chem. A* **104** 5660–94
- [3] Corkum P B and Krausz F 2007 Attosecond science *Nature Phys.* **3** 381–7
- [4] Kling M F and Vrakking M J J 2008 Attosecond electron dynamics *Annu. Rev. Phys. Chem.* **59** 463–92
- [5] Krausz F and Ivanov M 2009 Attosecond physics *Rev. Mod. Phys.* **81** 163–234
- [6] Weiner A M 2000 Femtosecond pulse shaping using spatial light modulators *Rev. Sci. Instrum.* **71** 1929–60
- [7] Weiner A M 2011 Ultrafast optical pulse shaping: a tutorial review *Opt. Commun.* **284** 3669–92
- [8] Brixner T, Krampert G, Pfeifer T, Selle R, Gerber G, Wollenhaupt M, Graefe O, Horn C, Liese D and Baumert T 2004 Quantum control by ultrafast polarization shaping *Phys. Rev. Lett.* **92** 208301
- [9] Köhler J, Wollenhaupt M, Bayer T, Sarpe C and Baumert T 2011 Zeptosecond precision pulse shaping *Opt. Express* **19** 11638–53
- [10] Autler S H and Townes C H 1955 Stark effect in rapidly varying fields *Phys. Rev.* **100** 703–22
- [11] Meier C and Engel V 1994 Interference structure in the photoelectron spectra obtained from multiphoton ionization of Na_2 with a strong femtosecond laser pulse *Phys. Rev. Lett.* **73** 3207–10
- [12] Wollenhaupt M, Liese D, Präkelt A, Sarpe-Tudoran C and Baumert T 2006 Quantum control by ultrafast dressed states tailoring *Chem. Phys. Lett.* **419** 184–90
- [13] Palacios A, Bachau H and Martín F 2006 Step-ladder Rabi oscillations in molecules exposed to intense ultrashort vuv pulses *Phys. Rev. A* **74** 031402

- [14] Bustard P J, Wu G, Lausten R, Townsend D, Walmsley I A, Stolow A and Sussman B J 2011 From molecular control to quantum technology with the dynamic Stark effect *Faraday Discuss.* **153** 321–42
- [15] Wollenhaupt M, Assion A, Bazhan O, Horn C, Liese D, Sarpe-Tudoran C, Winter M and Baumert T 2003 Control of interferences in an Autler–Townes doublet: symmetry of control parameters *Phys. Rev. A* **68** 015401
- [16] Frohnmeyer T, Hofmann M, Strehle M and Baumert T 1999 Mapping molecular dynamics (Na_2) in intense laser fields: another dimension to femtochemistry *Chem. Phys. Lett.* **312** 447–54
- [17] Trallero-Herrero C, Cohen J L and Weinacht T 2006 Strong-field atomic phase matching *Phys. Rev. Lett.* **96** 063603
- [18] Goto H, Katsuki H, Ibrahim H, Chiba H and Ohmori K 2011 Strong-laser-induced quantum interference *Nature Phys.* **7** 383–5
- [19] Sussman B, Townsend D, Ivanov M and Stolow A 2006 Dynamic stark control of photochemical processes *Science* **314** 278–81
- [20] Wollenhaupt M and Baumert T 2006 Ultrafast strong field quantum control on K_2 dimers *J. Photochem. Photobiol. A* **180** 248–55
- [21] Petersen J and Mitrić R 2012 Electronic coherence within the semiclassical field-induced surface hopping method: strong field quantum control in K_2 *Phys. Chem. Chem. Phys.* **14** 8299–306
- [22] Bayer T, Wollenhaupt M and Baumert T 2008 Strong-field control landscapes of coherent electronic excitation *J. Phys. B: At. Mol. Opt. Phys.* **41** 074007
- [23] Remacle F and Levine R D 2006 An electronic time scale in chemistry *Proc. Natl Acad. Sci. USA* **103** 6793–8
- [24] Neidel Ch *et al* 2013 Probing time-dependent molecular dipoles on the attosecond time scale *Phys. Rev. Lett.* **111** 033001
- [25] Bayer T, Braun H, Sarpe C, Siemering R, von den Hoff P, de Vivie-Riedle R, Baumert T and Wollenhaupt M 2013 Charge oscillation controlled molecular excitation *Phys. Rev. Lett.* **110** 123003
- [26] Braun H, Bayer T, Sarpe C, Siemering R, von den Hoff P, de Vivie-Riedle R, Baumert T and Wollenhaupt M 2013 Efficient attosecond control of electron dynamics in molecules *EPJ Web Conf.* **41** 02026
- [27] Wollenhaupt M, Präkelt A, Sarpe-Tudoran C, Liese D and Baumert T 2005 Strong field quantum control by selective population of dressed states *J. Opt. B* **7** 270
- [28] Bayer T, Wollenhaupt M, Sarpe-Tudoran C and Baumert T 2009 Robust photon locking *Phys. Rev. Lett.* **102** 023004
- [29] Bai Y S, Yodh A G and Mossberg T W 1985 Selective excitation of dressed atomic states by use of phase-controlled optical fields *Phys. Rev. Lett.* **55** 1277–80
- [30] Meshulach D and Silberberg Y 1998 Coherent quantum control of two-photon transitions by a femtosecond laser pulse *Nature* **396** 239–42
- [31] Herek J, Wohlleben R, Cogdell R, Zeidler D and Motzkus M 2002 Quantum control of energy flow in light harvesting *Nature* **417** 533–5
- [32] Wollenhaupt M *et al* 2006 Femtosecond strong-field quantum control with sinusoidally phase-modulated pulses *Phys. Rev. A* **73** 063409
- [33] von den Hoff Ph, Kowalewski M and de Vivie-Riedle R 2011 Searching for pathways involving dressed states in optimal control theory *Faraday Discuss.* **153** 159–71
- [34] Präkelt A *et al* 2003 Compact, robust and flexible setup for femtosecond pulse shaping *Rev. Sci. Instrum.* **74** 4950–3
- [35] Siegman A E 1986 *Lasers* (Sausalito, CA: University Science Books)
- [36] Mulliken R 1971 Role of kinetic energy in the Franck–Condon principle *J. Chem. Phys.* **55** 309–14
- [37] Assion A *et al* 1996 Femtosecond pump-probe photoelectron spectroscopy: mapping of vibrational wave-packet motion *Phys. Rev. A* **54** R4605–8
- [38] Baumert T *et al* 1991 Femtosecond time-resolved wave packet motion in molecular multiphoton ionization and fragmentation *J. Phys. Chem.* **95** 8103–10
- [39] Assion A *et al* 1997 Femtosecond time-resolved observation of above threshold ionization in Na_2 *Phys. Rev. A* **55** 1899–902
- [40] Manz J, Pérez-Torres J F and Yang Y 2013 Nuclear fluxes in diatomic molecules deduced from pump-probe spectra with spatiotemporal resolutions down to 5 pm and 200 asec *Phys. Rev. Lett.* **111** 153004
- [41] Wollenhaupt M and Baumert T 2011 Ultrafast laser control of electron dynamics in atoms, molecules and solids *Faraday Discuss.* **153** 9–26
- [42] Schneider J, Wollenhaupt M, Winzenburg A, Bayer T, Köhler J, Faust R and Baumert T 2011 Efficient and robust strong-field control of population transfer in sensitizer dyes with designed femtosecond laser pulses *Phys. Chem. Chem. Phys.* **13** 8733–46
- [43] de Vivie-Riedle R and Troppmann U 2007 Femtosecond lasers for quantum information technology *Chem. Rev.* **107** 5082–100